

Egyptian Journal of Chemistry

http://ejchem.journals.ekb.eg/



Hexavalent Chromium Removal Using Novel Magnetite-Functionalized Human Hair and Berseem Hay in Batch and Column Systems

Yasmin El-Dakrory^{1,2*}, Eman A. Ashour², Maha Abdelkreem³



¹Department of Basic science, Higher Technological Institute, 6th of October city, Postal code 4 Giza, Egypt.

²Department of chemical engineering, Faculty of Engineering, Minia University, 61516 Minia, Egypt. ³Department of chemical engineering, Higher Technological Institute, 10th of Ramadan city, Giza, Egypt.

Abstract

One of the alternatives for pollutants removal nowadays is nanotechnology. In this study, ferric nanoparticles (Fe₃O₄) loaded berseem hay (BH) and human hair (HH) to form magnetite nanoparticles (MNLBH and MNLHH) were used as efficient adsorbents to remove hexavalent chromium (Cr⁺⁶) from wastewater through batch and fixed-bed column adsorption. The zeta potential, TEM, FTIR, and XRD were employed to characterize the adsorbents. Adsorption experiments were conducted under varying conditions, including pH, contact time, adsorbent dosage, and initial metal concentration. At acidic medium, 100 ml of a 10 mg L⁻¹ concentrated solution was removed by 0.15 g of MNLHH in 60 minutes and by MNLBH in 70 minutes, with an efficiency of 94.5 % and 91%, respectively, of heavy metal Isotherm models indicated that Temkin best fit MNLHH data, while Langmuir described MNLBH well; kinetic studies followed pseudo-second-order and pseudo-first-order models, respectively. In column studies, Cr⁶ concentration (10–20 ppm), flow rate (2.5–3.5 mL/min), and bed height (0.3–1 cm) were varied, with maximum capacity reaching 3.142 mg/g at 0.5 cm. The study highlights a novel, eco-friendly, and cost-effective bio-composite for Cr⁶ remediation.

Keywords: MNLHH, MNLBH, Adsorption, hexavalent chromium, Fixed bed column, TEM; FTIR; and XRD, Isotherm.

1. Introduction

The influx of heavy metals into aquatic environments is a major cause for anxiety across the world. These hazardous pollutants have the potential to have devastating impacts on ecosystem services and human health. Chromium (Cr), nickel (Ni), arsenic (As), cobalt (Co), zinc (Zn), copper (Cu), and mercury (Hg) are all elements known to be poisonous heavy metals [1]. Metals are non-biodegradable and very prone to forming complexes, which can lead to extremely slow breakdown [2]. Industrial effluent containing large amounts of hexavalent chromium [Cr +6] has been released into the environment in recent decades, posing a serious hazard due to the mutagenic and carcinogenic effects, it has on living things. According to the World Health Organization (WHO), the maximum allowable concentration of Cr+6 in drinking water is 0.05 mg/L. Industrial waste containing Cr +6 cannot exceed 0.1 mg/L, according to the Minimal National Standards (MINAS) [3]. Chromium metals are discharged into the environment by many industries, including electroplating, animal skin tanning, paints, pigments, pulp processing, wood preservation, metal corrosion prevention, and steel manufacturing. They all release massive volumes of chromium-containing waste into the environment [4,5].

A number of technologies have been applied to the problem of wastewater treatment and water purification in the last several years. These technological advancements include both conventional techniques and novel strategies for purifying up polluted water sources [6]. There are a number of methods that have been employed to eliminate heavy metal ions, such as chemical precipitation, ion-exchange, adsorption onto activated carbon, membrane filtration (including ultrafiltration), and many more [7]. Adsorption is recognized as a low-cost and incredibly efficient method of removing heavy metals from polluted water [8]. Utilization of bio-adsorbents and commercial adsorbents with high removal capacities are both employed to extract heavy metals from wastewater [9]. Cellulosic biomaterials' hydroxyl functional groups make them effective adsorbents, that can be identified in agricultural byproducts [10]. Recent years have seen a surge in interest in metal oxide nanoparticles due to their intriguing physical, chemical, and catalytic properties.

Because of these characteristics, Fe₃O₄ MNPs have found use in many different fields, including the material, chemical, biological, and physical sciences [11]. In addition, it has gained significance in biological applications and environmental matrix treatments as a result of its function, adaptability, and stability [12].

In this context, the present study introduces a novel batch and fixed-bed column system using a magnetic nanocomposite synthesized from agricultural waste and Fe₃O₄ nanoparticles (MNLHH and MNLBH) for the efficient removal of Cr⁺⁶ from aqueous solutions. The synthesized MNLHH and MNLBH materials were thoroughly characterized using Transmission Electron Microscopy (TEM), Fourier Transform Infrared Spectroscopy (FTIR), Zeta potential analysis, and X-ray Diffraction (XRD). While prior research has examined magnetic composites and bio-adsorbents independently, the incorporation of human hair and berseem hay with magnetite (Fe₃O₄) nanoparticles represents a novel and underexplored approach. This study evaluates the adsorption performance of MNLHH and MNLBH through both batch and fixed-bed column experiments, offering detailed analysis of adsorption kinetics, isotherm models, and breakthrough behavior. By addressing common challenges related to cost and adsorbent separation, the research presents a promising advancement toward sustainable and scalable adsorption systems for wastewater treatment.

2. Materials and Methods

2.1 Chemicals

The following chemicals sulfuric acid (H₂SO₄, 98%), ferrous sulfate (FeSO₄.7H₂O), ferric chloride hexahydrate (FeCl₃.6H₂O), ammonia (30%), sodium chloride (NaCl), sodium hydroxide (NaOH), hydrochloric acid (HCl), Potassium dichromate (K₂Cr₂O₇), 1,5-Diphenyl carbazide (C₆H₅NHNHCONHNHC₆H₅) and acetone were used in the study and obtained from (Merk, Germany).

2.2. Sample preparation

A standard stock solution of hexa-chromium ion Cr⁺⁶ was prepared by dissolving 2.828 g of potassium dichromate (K₂Cr₂O₇) in 1000 mL deionized water. The experimental solutions (1,5, 7 and 10 mg L⁻¹) were outfitted by diluting the dye stock solution.

2.3. Preparation of the adsorbents

2.3.1. Preparation of magnetite nanoparticles loaded berseem hay (MNLBH)

Berseem hay was collected from farmers' fields. After collection berseem hay was washed with tap water and distilled water several times to remove dust and impurities. Washed sample was air dried and crushed into small pieces. Afterwards, it was sieved in a size range $90 \mu m$.

Ferrous sulfate (3.33 g) and ferric chloride (6.47 g) were dissolved in double distilled water (DDW) with vigorous stirring for 30 min. Then 5 g of berseem hay was added into the mixture while stirring for 3 h. Chemical co-precipitation was achieved at 30 °C under vigorous stirring by gradually adding 30 mL of NH₃ solution (30% by wt.). The color of the suspension changed from dark brown to black. The pH of the residual was maintained at around 10 during the reaction process. The reaction system was kept at 70 °C for 1 h then cooling to room temperature. The black solid precipitate (MNLBH nanocomposite) was subsequently collected by a magnet and repeatedly rinsed with water several times, and with 0.02 moL⁻¹ sodium chloride two times. Eventually, the as-synthesized MNLBH nanocomposite was dried at 45°C for 12 h.

2.3.2. Preparation of the Magnetite Nanoparticles Loaded Human Hair (MNLHH) adsorbent.

Hair waste was collected from local barbershops, with samples obtained from male individuals approximately twelve years old. The gathered hair was initially combined, thoroughly cleaned using a standard laboratory detergent, and rinsed multiple times with double-distilled water. It was then dried at 80°C for 10 h. Once completely dry, the hair was ground and sieved to achieve a particle size of 90 µm [13].

The synthesis of Fe₃O₄ nanoparticles loaded with human hair was carried out using a modified co-precipitation method. A solution containing 3.33 g of FeSO₄·7H₂O, 6.47 g of FeCl₃·6H₂O, and 150 ml of DDW was stirred vigorously for 30 minutes. Following this, 5 g of waste human hair was introduced into the solution and continuously agitated for 3 h. Ammonia solution (30% by weight) was gradually added under constant stirring, leading to a chemical co-precipitation reaction at 30°C. A noticeable color shift from orange to black was observed. During the reaction, the solution's pH was consistently maintained at approximately 10, while the system was kept at 70°C for 1 hour. Afterward, the MNLHH was repeatedly washed with DDW and twice with 0.02 mol L⁻¹ sodium chloride before being dried at 45°C for 12 h. The integration of magnetic nanocomposites into the MNLHH process resulted in exceptional magnetic properties.

2.4. Characteristic techniques

The USB-650 UV-VIS Red Tide Spectrometer (Ocean Optics Inc.) is a compact, USB-powered device specifically designed for UV-Visible absorbance measurements. It operates across a wavelength range of 200–850 nm and features a 2048-element CCD array detector, offering a spectral resolution of approximately 2.0 nm. With a signal-to-noise ratio of 250:1, an integration time ranging from 3 ms to 10 s, and a dynamic range of 8×10^7 , the device interfaces via USB 2.0 and is operated using Oceanview software for data collection and analysis. In this study, the spectrometer was integrated with a USB-ISS-UV/VIS sampling system to monitor the UV-Vis absorbance of Cr^{+6} at 540 nm, enabling evaluation of adsorption efficiency.

(TEM) was conducted using a JEOL JEM-2100F-HR (Japan), operated at an accelerating voltage of 200 kV. The instrument provides high-resolution imaging up to 0.1 nm and magnification levels of up to 800,000, which was employed to examine the surface morphology of the synthesized adsorbent. (XRD) analysis was performed using an Empyrean diffractometer (USA), equipped with a Cu Kα radiation source (λ = 1.5406 Å) operating at 45 kV and 30 mA. Diffraction patterns were recorded within the 2θ range of 5°-80° to assess the crystallinity of the sample and confirm the incorporation of Fe₃O₄ nanoparticles

The point of zero charge (pH_{pzc}) was determined using the salt addition method. A 20 mL solution of 0.01 mol L⁻¹ NaCl was prepared and its initial pH (pH_i) was adjusted between 1 and 9 using 0.1 M HCl or 0.1 M NaOH. After 30 minutes of stirring, 0.05 g of MNLHH or MNLBH was added, and the final pH (pH_f) was measured. The pH_{pzc} was identified at the point where the difference (pH_i - pH_f) equaled zero [14,15]. (FTIR) spectroscopy was carried out using a PerkinElmer Spectrum One FTIR spectrometer (USA) to identify functional groups and chemical moieties on the adsorbent surface. Spectra were collected in the range of 4000–400 cm⁻¹ using a high-sensitivity detector and either KBr pellet or ATR sampling techniques. The instrument offers a spectral resolution of up to 0.5 cm⁻¹, with an integrated interferometer and broadband infrared source, enabling precise detection of chemical bonds and molecular interactions. FTIR analysis provided insights into surface modifications, functional group dynamics, and chemical transformations before and after the adsorption process

2.5. Experimental procedures

2.5.1. Batch experimental

onto the MNLHH surface.

Adsorption studies have been performed by combining 100 mL of Cr⁺⁶ solution with 0.2 g of MNLBH and MNLHH in separate volumes, and then vigorously agitating the mixture. Room temperature (25 ± 2 °C) was used to test the effects of predetermined Cr⁺⁶ concentrations, adsorbent dosages (0.05, 0.1, 0.15, and 0.2 g/ 100 ml), pH, and contact time. Samples of the Cr⁺⁶ solution was removed from the adsorbent magnetic separation process at various intervals caused by the external magnetic field. Using 1, 5-diphenylcarbazide as a complexing agent, a colorimetric approach was employed to determine the remaining concentration of Cr ⁺⁶ at 540 nm (λ_{max}) in the aqueous solution using a spectrophotometer equipped with UVvisible spectroscopy was used for testing these samples. Equations for Cr⁺⁶ adsorption capacity was calculated by the following equation [16]:

$$q_e = \frac{(C_0 - C_e)V}{M} \tag{1}$$

Where, q_e is the equilibrium adsorption capacity (mg. g^{-1}), C_o and Ce are the initial and equilibrium concentrations of heavy metal (mg L^{-1}), V is the volume (L), and M is the weight (g) of the adsorbent. It should be noted that the equilibrium concentration of sodium fluorescein in the aqueous solutions was determined according to the absorbance measured by (UV-Visible absorption spectroscopy) in the light of the Beer-Lambert relation The efficiency of pollutant removal (%) was calculated using the following equation:

Pollutant removal efficiency =
$$\frac{(C_o - C_t)}{C_o} \times 100$$
 (2)

where $C_t \text{ (mg L}^{-1}\text{)}$ is Cr^{+6} concentration at time t (min).

2.5.2. Continuous experimental (fixed bed column)

Continuous adsorption experiments were performed using specific quantities of MNLHH and MNLBH separately packed into a cylindrical glass column measuring 1 cm in diameter and 25 cm in height. The adsorbent was tightly packed within the column, with layers of glass wool positioned at both ends of the bed to ensure uniform liquid dispersion. Bed heights of 0.3 cm, 0.5 cm, and 1 cm were achieved by varying the MNLHH or MNLBH loading accordingly. A peristaltic pump (Watson Marlow, England) delivered Cr⁺⁶ solution at controlled flow rates of 2.5 and 3.5 mL/min. The influent Cr⁺⁶ concentrations were maintained at 10 and 20 ppm, with the pH fixed at 2. Effluent samples were collected at consistent time intervals over a 510-minute period. The Cr⁺⁶ concentration in the samples was analyzed to monitor adsorption performance, and breakthrough curves were generated to determine when the adsorbent became saturated. The adsorption process was considered complete when the effluent dye concentration reached 99.5% or more of the initial influent level [17,18].

2.5.3. Column data analysis

In order to predict the fixed-bed column's performance, breakthrough curves were used. Time to breakthrough and form of the break-through curve are crucial factors for understanding the operation and dynamic responsiveness of a sorption column. The breakthrough curve for a specific bed depth is often represented by the ratio C_VC_0 , which indicates the concentration of a substance in the effluent relative to its initial concentration, as a function of time or volume. The effluent volume, Veff (in milliliters), may be determined from the relation [19]:

$$V_{eff} = Qt_{total} \tag{3}$$

Where, Q is the volumetric flow rate (mL min. $^{-1}$) and t_{total} is the total flow time (min.).

The total mass of dye adsorbed, q_{total} (mg), can be calculated from the area under the breakthrough curve:

$$q_{total} = \frac{Q}{1000} \quad \int_{t=0}^{t=total} C_{ad} \ dt \tag{4}$$

Where, C_{ad is} the concentration of dye removal (mg/L).

Equilibrium dye uptake or maximum capacity of the column, $q_{e,exp}$ (mg g) is defined by:

$$q_{e.exp} = \frac{q_{\text{total}}}{m} \tag{5}$$

Where, m is the dye weight of adsorbent in the column (g).

Total amount of metal ion entering to the column (m_{total}) is calculated from the following equation:

$$m_{total} = \frac{C_0 q_{total}}{1000} \tag{6}$$

The adsorption rate and the influent flow rate affect the mass transfer zone (MTZ) length. The length of the MTZ may be computed as follows:

$$L_{MIZ} = L \frac{t_e - t_b}{t_e} \tag{7}$$

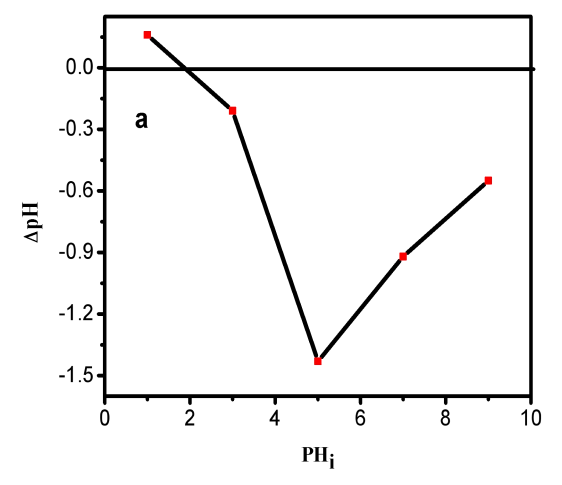
Where, L is the height of the bed (cm) and t_b is the time (min.) that is desired to reach the breakthrough point and t_e (min.) is the time of exhaustion [20].

3. Results and Discussion

3.1. Characterization of the prepared adsorbent

3.1.1. Zeta potential

Measuring the pH of zero-point charge (pH_{ZPC}) is necessary for determining the optimum pH value of heavy metals-polluted wastewater for adsorption. The point of zero-charge (pH_{PZC}) for adsorbents MNLBH and MNLHH were found to be 1.89 and 1.32, respectively, based on the results reported in Fig. 1. The active sites on the biosorbent surface had a positive charge at pH values below the pH_{PZC} and a negative charge at pH values above the pH_{PZC}.



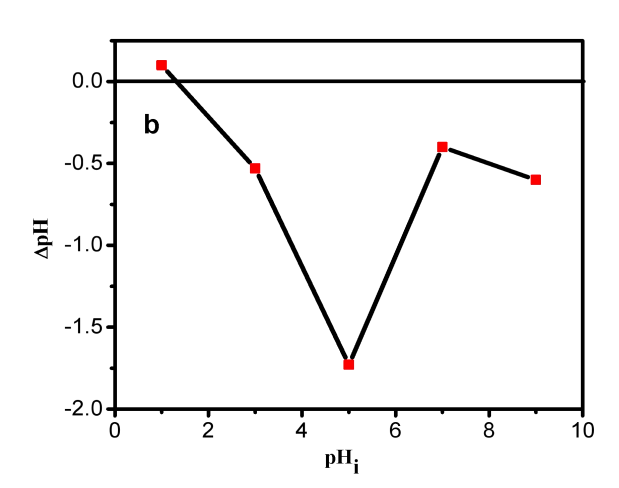


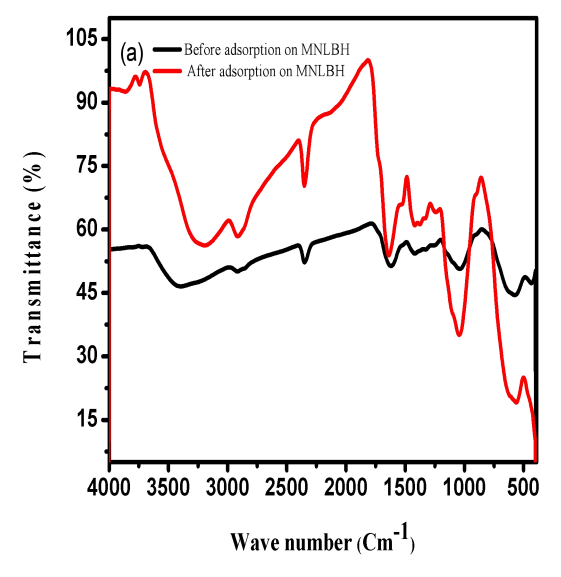
Fig. 1. Point of zero charge for a) MNLBH and b) MNLHH

3.1.2. FTIR characterization

The FTIR method was used to identify the chemical molecules affixed to the surface of the magnetite nanoparticles that were incorporated into berseem hay and human hair. As shown in Fig. 2.a., these were carried out both before and after the Cr⁺⁶ was applied. For MNLBH the spectrum region of 3935.86 to 3743.12 cm⁻¹, characteristic bands were discovered, which align with the O-H group associated with alcohol/phenol functionality [21]. Bands in the 2918.22–2350.99 cm⁻¹ spectral region was identified as C-H groups of methyl and methylene. Further, the presence of amines, carbonyl groups, and oxygen-containing groups on the surface of MNLBH is demonstrated by bands at 1619.06 cm⁻¹ and 1261.89 cm⁻¹, which correspond to the C-N and C-O bonds, respectively. The important finding of a 573.55 cm⁻¹ vibration peak that corresponds to the Fe-O bond strongly implies that the MNLBH contains iron oxides [22]. Modifications to the spectrum are noticeable as a result of Cr⁺⁶ adsorption on the MNLBH surface that has been loaded with Cr⁺⁶. Surface hydroxyl groups' involvement in Cr⁺⁶ adsorption is confirmed by the band's shift from 3718.21 to 3743.12 cm⁻¹ and the corresponding rise in intensity. Also, we can see that the strength of various bands has changed and shifted, particularly at (573.55, 1038.78, 1261.89, 1619.39 cm⁻¹), which has moved

to (561.85,1044.25, 1240.38, 1638.68 cm⁻¹), respectively. Cr⁺⁶ and MNLBH interact to cause these variations in intensity and wavenumbers.

Otherwise, in Fig. 2.b. the MNLHH spectra revealed the stretching vibrations of -OH and -NH based on prominent peaks at 3717-3416 cm-1. The large absorption peaks are largely formed by amino acid-hydroxyl group hydrogen bonding [23]. Methyl (CH₃) has a C-H asymmetric mode absorption band at 2921 cm⁻¹. At a width of 1632 cm⁻¹, the Amide I band represents the in-plane bending of N-H and C-N stretching modes, linked to the functional group C = O stretching. Amide II absorbs at 1538 cm⁻¹ due to C-H and N-H stretching. From the -COO- group, the -CO absorption band was 1438 cm⁻¹. Beamide III was identified by a weak band at 1247 cm⁻¹, which was connected to a complicated vibration comprising N-H inplane, C-O, and O=C=N bending and stretching [24]. At 435 cm⁻¹, disulfide bonds (Cysteine S-S bonds) exhibit noticeable stretching vibrations [25]. The existence of a significant absorption band at 573.12 cm⁻¹, induced by Fe-O bond vibrations, indicates Fe₃O₄ nanoparticle formation [26]. Fig. 2.b before and after adsorption of Cr⁺⁶ on MNLHH shows discernible changes in the positions and intensities of some bands, particularly those at (3717, 1643.9,573.12 cm⁻¹), which change to (3745.15, 1649.21, and 566.73 cm⁻¹), respectively. The interactions between MNLHH and cr⁺⁶ is responsible for these variations in intensity and wavenumbers.



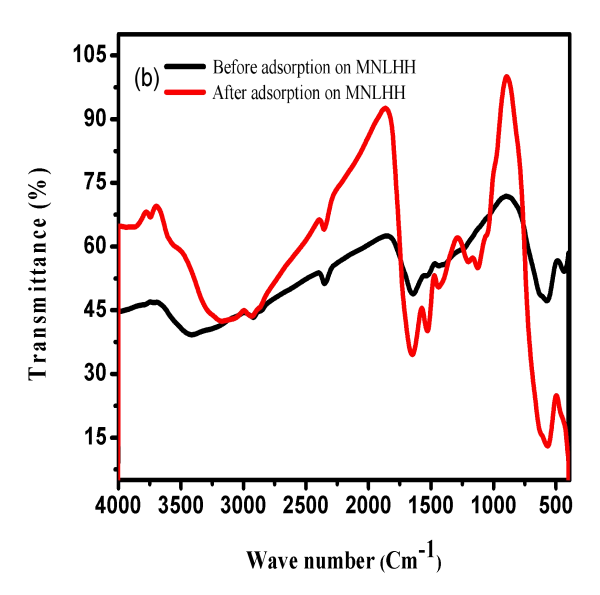
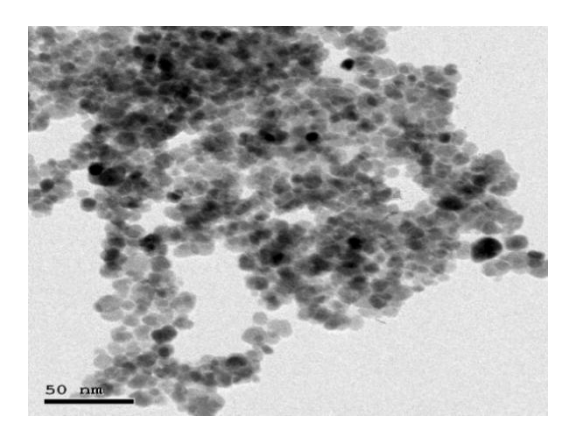
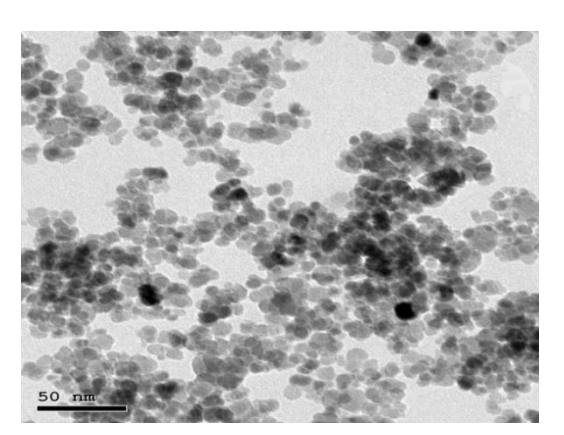


Fig. 2. a) FTIR spectra for MNLBH before and after Cr⁺⁶ adsorption and b) FTIR spectra for MNLHH before and after Cr⁺⁶ adsorption

3.1.3. TEM

TEM results verified that the produced (MNLBH) or (MNLHH) exhibited a spherical morphology, as shown in Fig. 3 (a) at 50 nm and in Fig. 3(b) at 100 nm. The size of the MNLBH ranged from 0.832 to 13.529 nm, whereas the size of the MNLHH varied from 1.8 to 31.8 nm. You can see the average size of MNLBH or MNLHH in Fig. 3 (c), which is 6.75 or 11.7 nm. The particles exhibited the absence of widespread aggregation in water and exhibited a lack of heterogeneity in their spherical to platelet-shaped distribution.





Egypt. J. Chem. 69, No. 2 (2026)

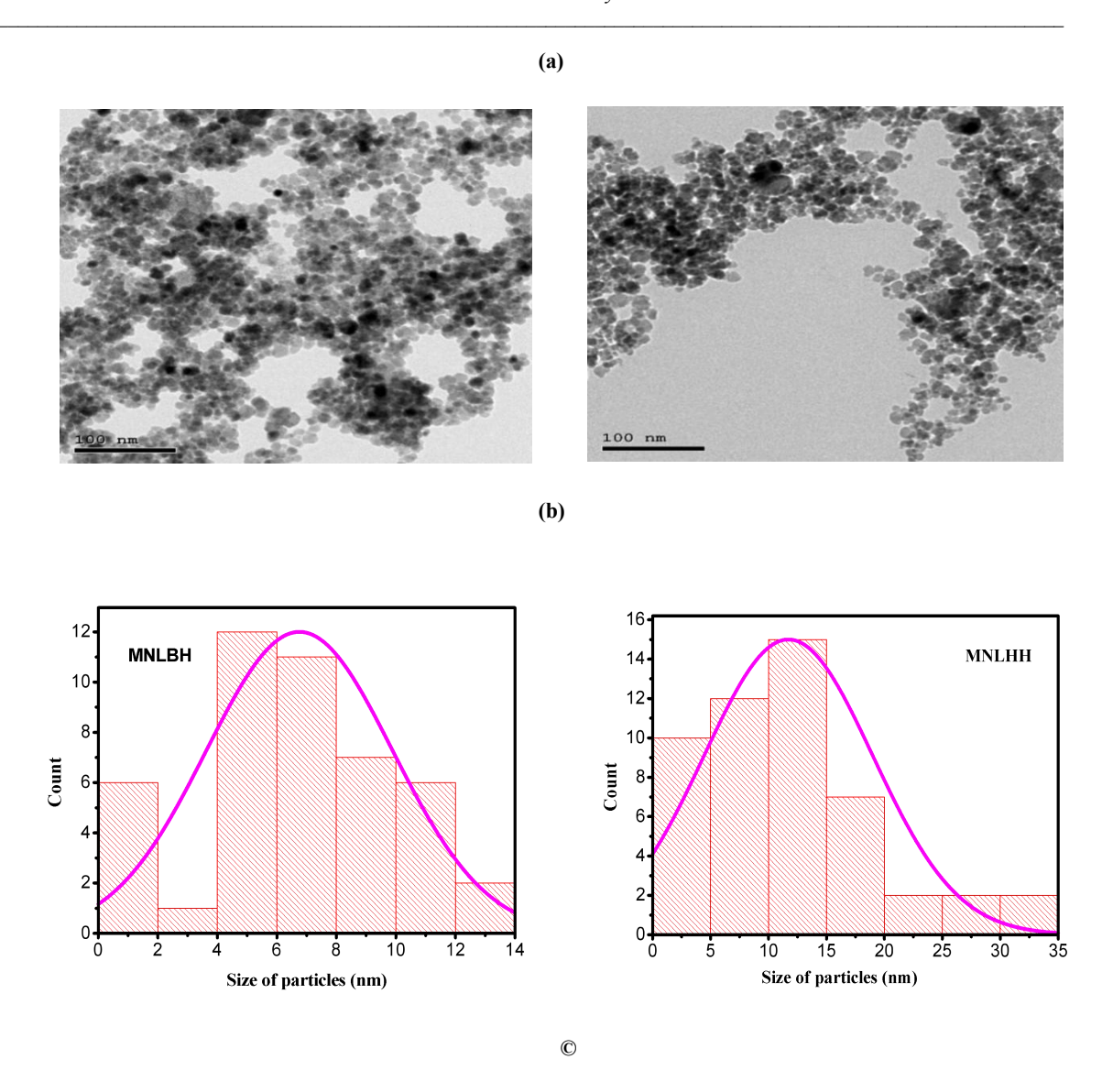


Fig. 3. TEM image of MNLBH and MNLHH at (a) 50 nm, (b) TEM image of MNLBH and MNLHH at 100 nm and

(c) average mean size nm of MNLBH and MNLHH

3.1.4. XRD

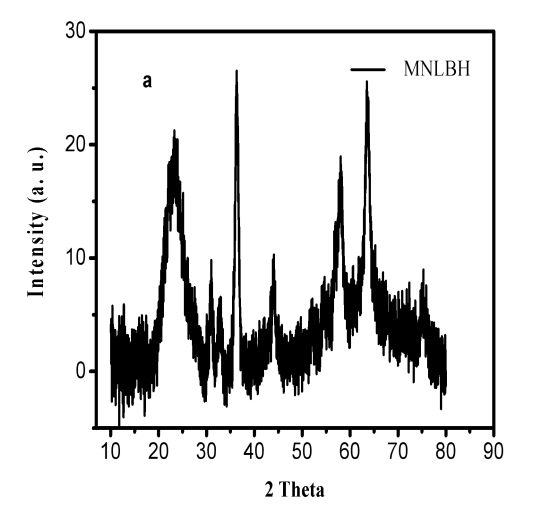
(XRD) analysis was employed to confirm the magnetic crystalline structure of the synthesized nanocomposite and to evaluate any structural changes resulting from surface modification. The XRD patterns of (MNLBH) and (MNLHH) are presented in Fig. 4. Characteristic diffraction peaks corresponding to Fe₃O₄ were observed at 2θ values of 30.3°, 35.7°, 43.5°, 53.8°, 57.2°, 62.8°, and 74.5°, indicating the presence of magnetite. All diffraction peaks corresponded precisely with the typical Fe₃O₄ diffraction data [27].

3.2. Batch adsorption study of chromium removal

3.2.1. Effect of pH

The adsorption process is greatly affected by the pH change, which affects the surface binding sites and charges on the adsorbent. The pH range for both adsorbents is 2 to 9. At a fixed contact period of 20 minutes and an initial Cr⁺⁶ concentration of 10 ppm, the pH values were obtained using 1N HCl and 1N NaOH. Fig .5 illustrates the process of Cr⁺⁶ absorption onto MNLHH and MNLBH as a result of pH diversity. At pH 2, the removal efficiencies of magnetite nanoparticles loaded on human hair (MNLHH) and berseem hay (MNLBH) were 94.5% and 91%, respectively. Apparent decreased removal efficiency was observed when pH increased. As the pH of the Cr⁺⁶ solution changes, the adsorbents' surface becomes less polar, which results in higher absorption at low pH. Cr⁺⁶ is found in aqueous solution in a number of forms, including H₂CrO₄, HCrO₄ · CrO₄ ·

Egypt. J. Chem. 69, No. 2 (2026)



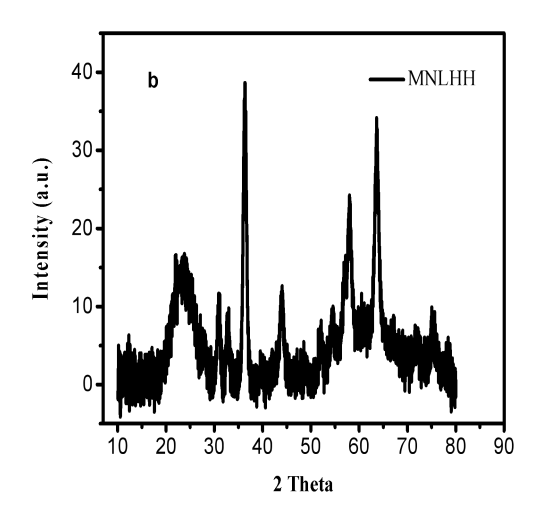


Fig. 4. XRD pattern of a) MNLBH and b) MNLHH

3.2.3. Effect of adsorbent dosage

The influence of adsorbent dose on chromium adsorption at 25 °C is demonstrated in Fig. 6. Results indicate that the % removal of chromium escalates with a higher adsorbent dosage. As the adsorbent dosage was elevated from 0.05 to 0.2 g, the percentage of chromium removal excesses from 68.5% to nearly 94.5% for MNLHH and from 25.5% to 91% for MNLBH. This transpires as a result of the availability of active binding sites with an elevated adsorbent dosage. Previously published observations indicate that a reduction in adsorbent capacity may occur owing to the aggregation of adsorbent particles and the presence of unbound sites within the adsorbents. Consequently, the active sites cannot bind metal ions [29,30].

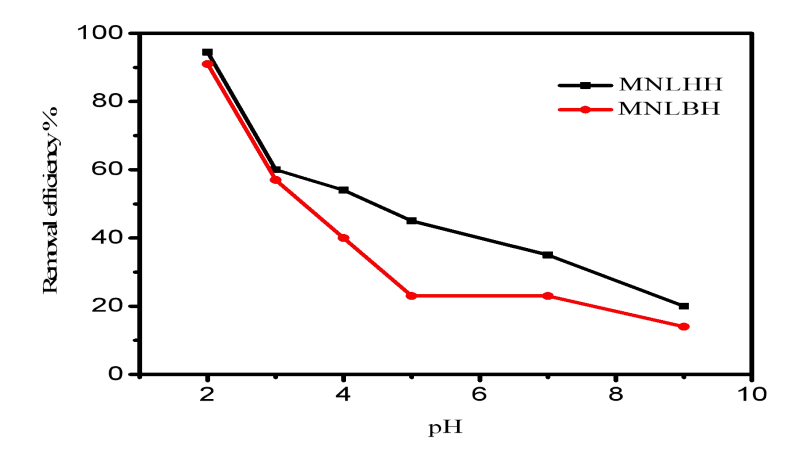


Fig. 5. Effect of pH on the Cr⁺⁶ removal by MNLHH and MNLBH (initial conc.10 mg L⁻¹, amount of adsorbents 0.15g and contact time 20 min.)

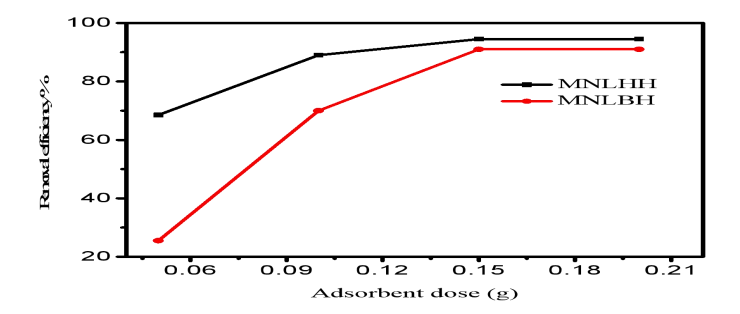


Fig. 6. Effect of the adsorbent dose on the Cr^{+6} removal by MNLHH and MNLBH (initial conc. 10 mg L^{-1} and pH = 2)

3.2.4. Impact of contact time and initial concentration

At the specified concentrations, the contact time parameter efficiently controls the removal of Cr^{+6} by MNLBH and MNLHH from aqueous solutions, as shown in Fig. 7. It was discovered that the adsorption uptake for Cr^{+6} by MNLHH was more than that by MNLBH, as the equilibrium point of Cr^{+6} adsorption for MNLHH is 3.26 mg. g^{-1} at 60 minutes and 3 mg. g^{-1} at 70 minutes. The rate of metal removal was initially greater due to the bigger adsorption surface area. At equilibrium, the adsorbent occupies all active sites [31,32].

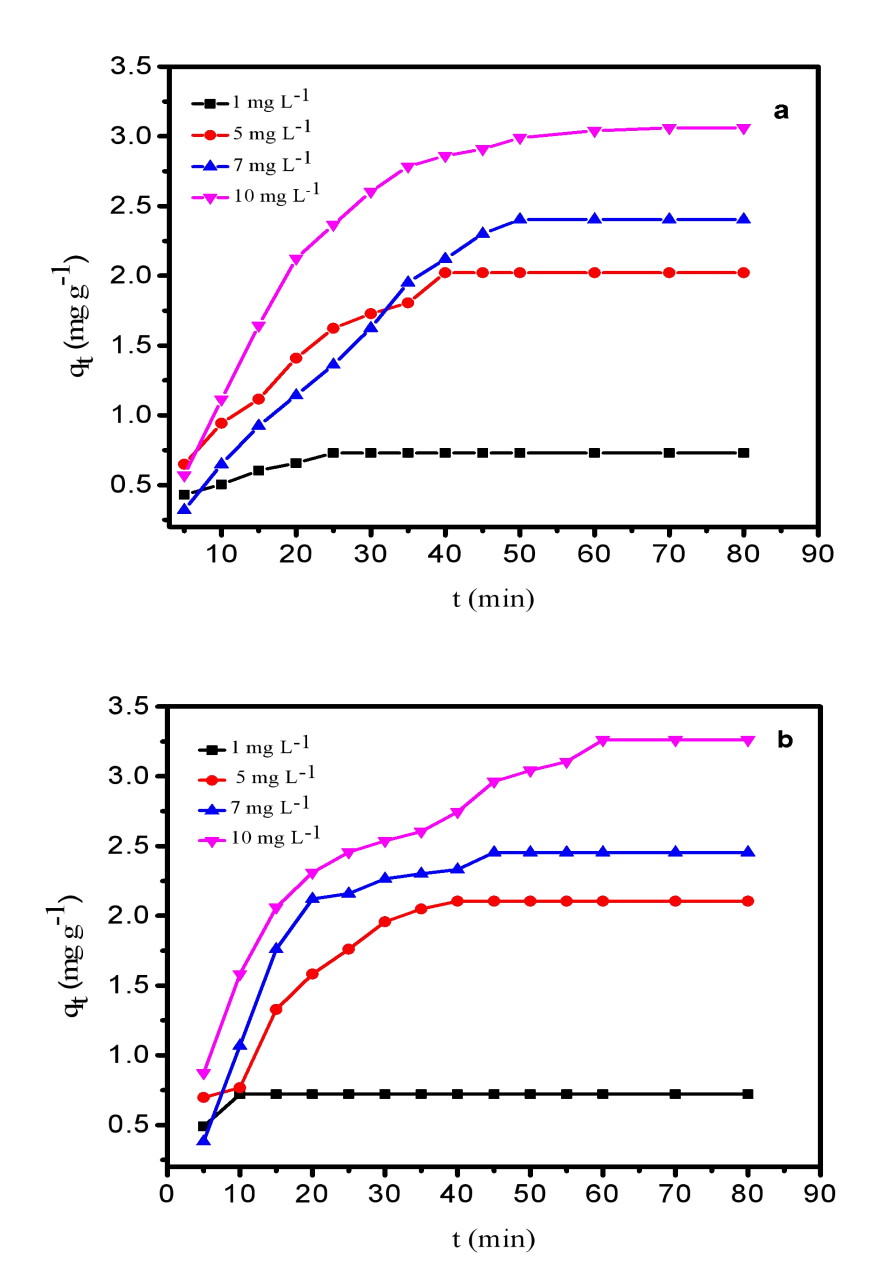


Fig. 7. Effect of the contact time on the Cr^{+6} removal by MNLHH and MNLBH (pH = 2 and amount of adsorbents = 0.15 g)

3.3. Adsorption Isotherms

A research study was conducted on the equilibrium data of the magnetite nanoparticles loaded berseem hay and human hair using the Freundlich, Temkin and Langmuir models. These models are mathematical systems that take into account parameters like adsorbent homogeneity/heterogeneity, species interaction, and coverage type during the adsorption process. These isotherms help us understand how the system operates, how effectively the adsorbent works, and whether the process is

economically viable. The Langmuir, Freundlich and Temkin isotherm models' linear equations are provided in Eqs. 8, 9 and 10, respectively [33].

$$\frac{1}{q_e} = \frac{1}{b C_e q_{max}} + \frac{1}{q_{max}}$$

$$\ln q_e = \ln K_f + \frac{1}{n} \ln C_e$$

$$q_e = B \ln K_T + B \ln C_e$$
(10)

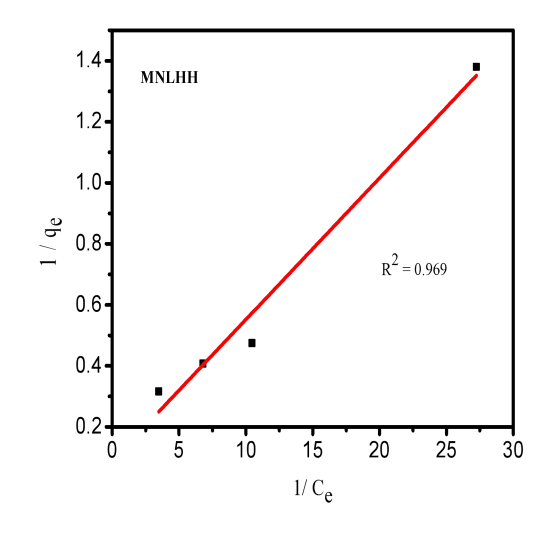
$$\ln q_e = \ln K_f + \frac{1}{n} \ln C_e \tag{9}$$

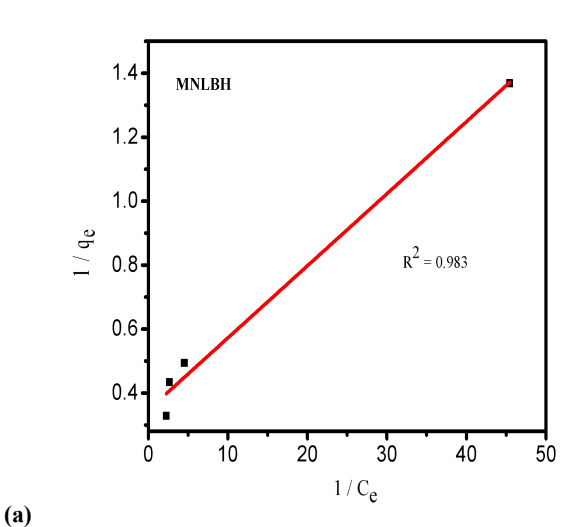
$$q_e = B \ln K_T + B \ln C_e \tag{10}$$

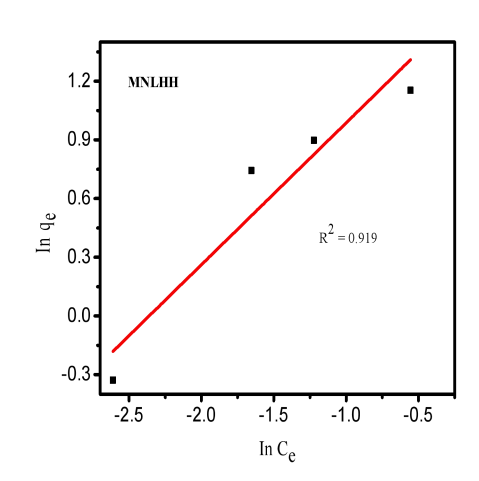
Whereas b (L mg⁻¹) is the Langmuir adsorption constant associated with the free energy of adsorption, q_e (mg g⁻¹) is the equilibrium capacity of dye on the adsorbent, and q_{max} (mg g⁻¹) is the adsorbent's maximum adsorption capacity. The capacity and intensity of adsorption are measured by the Freundlich constants $k_T (\text{mg}^{1-1/n} \text{ g}^{-1} \text{ L}^{1/n})$ and n respectively. Additionally, B = RT/b_T, where K_T is the Temkin isotherm constant (L mg⁻¹), b_T is the Temkin constant associated with heat of adsorption (J mol⁻¹), T (K) is the absolute temperature, R (8.314 J mol⁻¹K⁻¹) is the gas constant and B is associated with heat of adsorption [34]. In summary, Table 1 and Fig. 8 show the parameters that were computed using the Langmuir (Fig. 8(a)), Freundlich (Fig. 8(b)) and Temkin (Fig. 8(c)) equations. Because the sites on the adsorbent surface are evenly distributed, the Langmuir model is shown to have the greatest match for the adsorption of Cr⁺⁶ on MNLBH. Furthermore, the isotherm of Temkin shows that the adsorption via MNLHH is well conformed since the binding energies are well distributed.

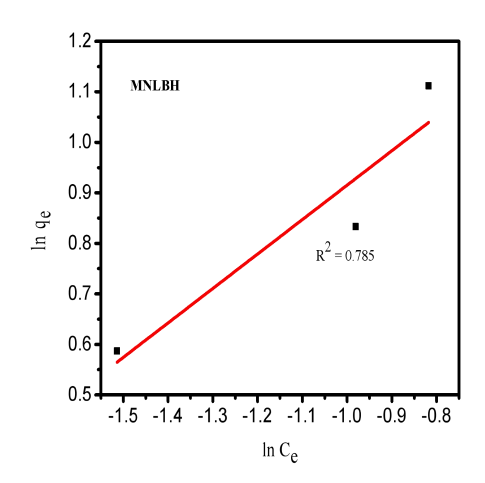
Table 1. Isotherm parameters for the adsorption of Cr⁺⁶ onto MNLHH and MNLBH

Adsorbent	Langmuir			Freundlish			Temkin		
MNLHH	В	q_{max} (mg g ⁻¹)	\mathbb{R}^2	n	$ m K_f \ (mg^{-1-1/n}g^{-1}L^{1/n})$	\mathbb{R}^2	В	K_T (L mg ⁻¹)	\mathbb{R}^2
MNLBH	1.901 15.43	11.36 2.882	0.969 0.983	1.434 1.467	8.379 4.933	0.9193 0.785	1.186 0.7153	46.478 95.582	0.9945 0.8774

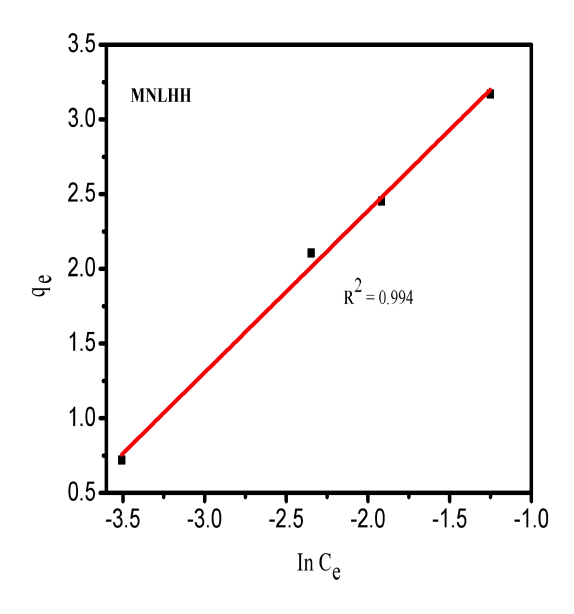








(b)



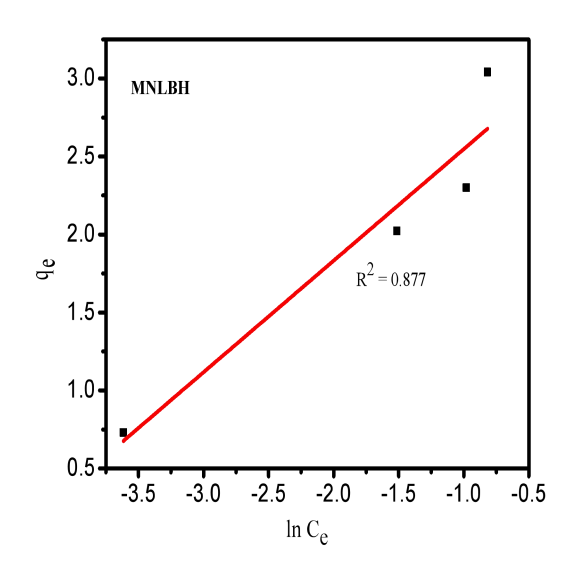


Fig. 8. Adsorption isotherms of Cr⁺⁶ in using (a) Langmuir, (b) Freundlich, and (c) Temkin models; in case MNLHH and MNLBH for diff erent concentrations.

(c)

3.4. Adsorption kinetics studies

Time-dependent adsorption investigations elucidate the adsorption rate and mechanism through experimental data analysis. An exhaustive examination of kinetic data is crucial for a more precise comprehension of the adsorption process. Consequently, to examine the interaction routes between Cr⁺⁶ and MNLBH or MNLHH, the adsorption data were analyzed utilizing pseudo-first-order, and pseudo-second-order, with the linear equations of each model articulated as follows [35,36].

$$log (q_e - q_t) = log q_e - \left(\frac{k_1}{2.303}\right)t$$

$$\frac{t}{q_t} = \frac{1}{k_2 q_e^2} + \frac{t}{q_e}$$
(12)
where, k_1 and k_2 are the pseudo-first and pseudo-second order kinetic model rate constants, while q_t (mg g⁻¹) is the adsorption

where, k_1 and k_2 are the pseudo-first and pseudo-second order kinetic model rate constants, while q_t (mg g⁻¹) is the adsorption capacity at time t. The related kinetic parameters in relation to the two models are provided in Table 2 and Fig. 9. The pseudo-second-order kinetic model provided the best match to the data on Cr^{+6} adsorption by MNLHH. This model indicates that chemisorption is the rate-limiting phase between the adsorbent and adsorbate, while pseudo-first-order kinetic model was fitted for adsorption of Cr^{+6} on MNLBH which implies that physical adsorption is a crucial component in influencing adsorption rates [37].

Table 2: Adsorption kinetic parameters for the adsorption of Cr+6 onto MNLHH and MNLBH adsorbents

Initial metal	Pseudo-fi	rst-order kine	tic model	Pseudo-second-order kinetic model			
concentration (mg L ⁻¹)	<i>K</i> ₁ (min ⁻¹)	\mathbb{R}^2	$q_e(\mathrm{mg}\;\mathrm{g}^{\text{-}1})$	K ₂ (g mg ⁻¹ min ⁻¹)	\mathbb{R}^2	<i>q</i> _e (mg g ⁻¹)	
(I) MNLTW							
1	0.228	-	0.7201	1.775	0.863	0.720	
5	0.106	0.927	3.515	0.0114	0.986	3.472	
7	0.083	0.947	2.603	0.0117	0.968	3.584	
10	0.063	0.928	3.398	0.0145	0.992	3.984	
(II) MNLBH							
1	0.095	0.9708	0.5241	0.168	0.976	0.894	
5	0.056	0.986	2.072	0.015	0.963	2.973	
7	0.0509	0.923	3.206	0.001	0.921	7.552	
10	0.0686	0.988	3.847	0.008	0.9603	4.368	

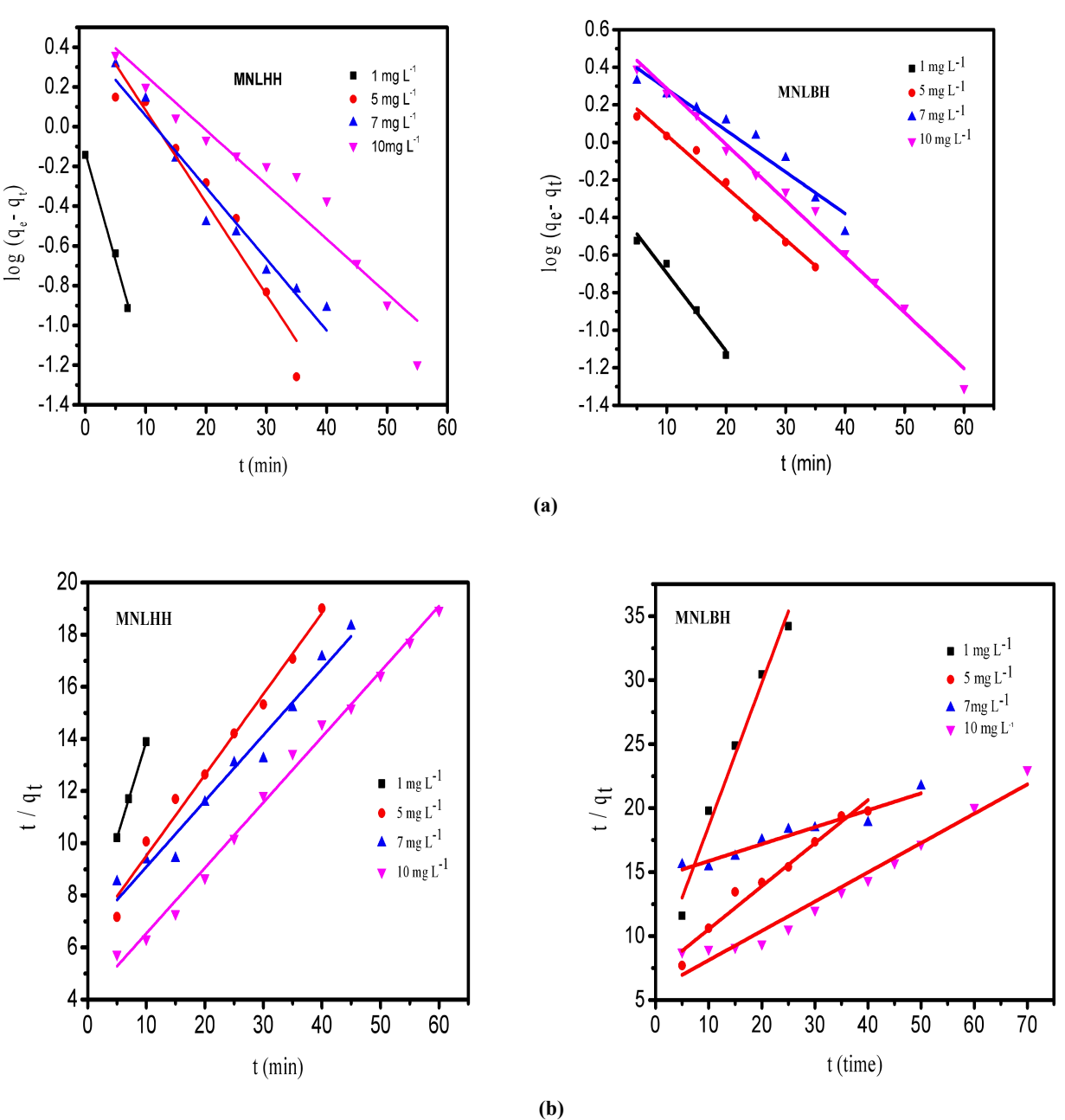


Fig. 9. Adsorption kinetics of Cr⁺⁶ in using (a) Pseudo first order and (b) Pseudo second order; in case of MNLHH and MNLBH for different concentrations.

3.5. Fixed bed adsorption study of Cr⁺⁶ removal 3.5.1. Effect of bed depth

The effect of different bed heights (0.3, 0.5, and 1 cm) on the removal of Cr⁺⁶ ions in a dynamic adsorption system are seen in Fig. 10. It is clear from the numbers that summarized in table 3, the breakthrough point and the adsorbent exhaustion period are affected by the bed height of the adsorption columns. The reason behind this is that the surface area increases as the amount of adsorbent in the column increases. The adsorption column data showed that adsorption capacities at bed heights (0.3, 0.5, and 1 cm) are 2.404, 3.142, and 3.018 mg g⁻¹ respectively. Increases in bed height of 0.3 to 1 cm were also connected with an increase in breakthrough time of 100 to 450 minutes. The mass transfer zone ranged 0.288 to 0.953 cm in length. The mass-transfer zone's enlargement caused the breakthrough curve's slope to decrease with increasing bed height [38,39].

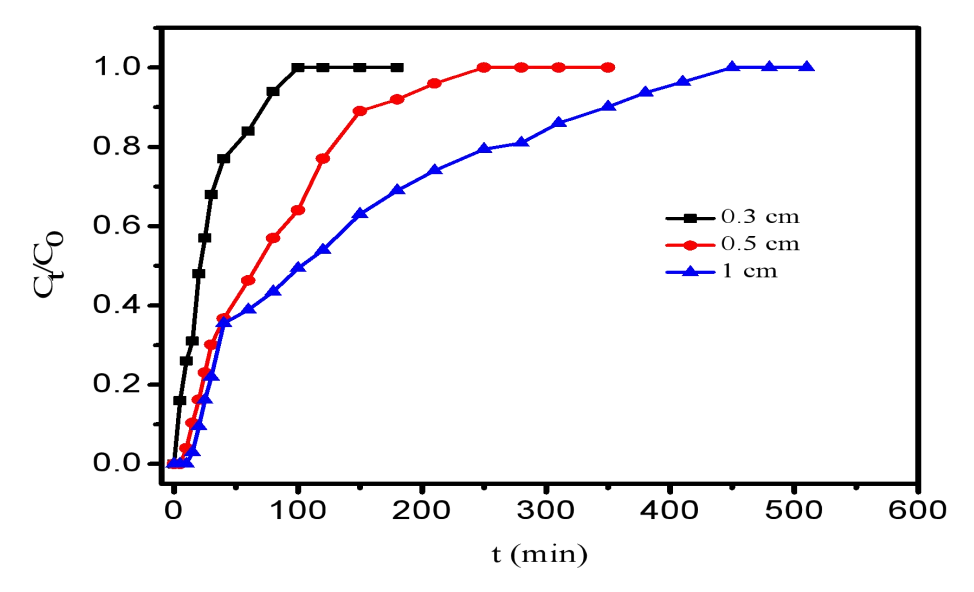


Fig. 10. Breakthrough curves at different bed depth (initial conc. = 10 mg L-1 and flow rate = 2.5 ml/min.)

3.5.2. Effect of flow rate

The flow rate of the influent solution is a critical parameter influencing the efficiency of heavy metal adsorption in fixed-bed columns. Recent studies have demonstrated that increasing the flow rate generally leads to a decrease in adsorption capacity and a shorter breakthrough time. This is primarily due to the reduced contact time between the heavy metal ions and the adsorbent, limiting the opportunity for effective mass transfer and adsorption. According to table (3) and Fig. 11, the Cr⁺⁶ exhaustion time decreased from 250 to 80 minutes when the flow rate increased from 2.5 to 3.5 mL min⁻¹[40].

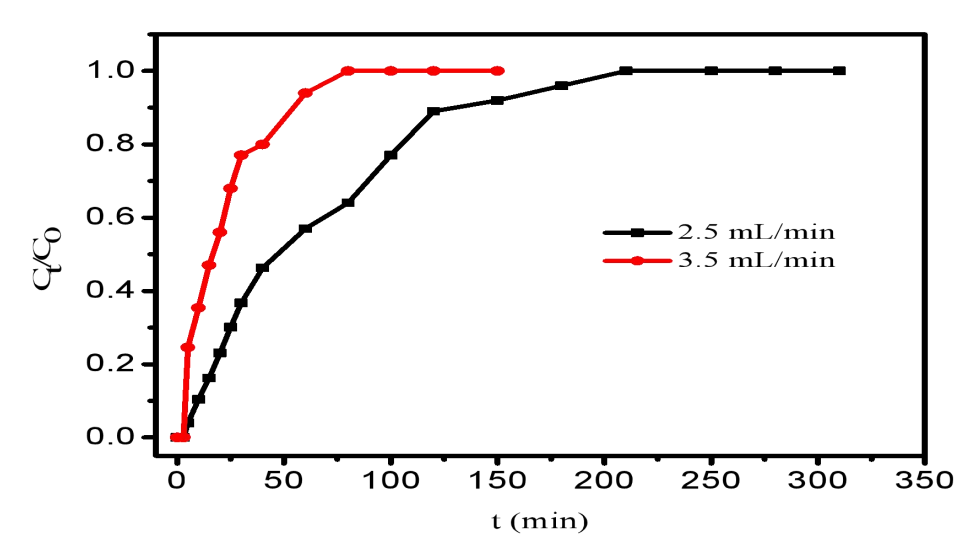


Fig. 11. Breakthrough curves at different flow rates (initial conc. = 10 mg L⁻¹ and bed depth = 0.5 cm)

3.5.3. Effect of initial concentration

 Cr^{+6} breakthrough curves at 10 and 20 mg L^{-1} influent concentrations are depicted in Fig. 12 and table 3. Flow velocity is maintained at 2.5 mL min⁻¹, and bed depth is 0.5 cm. As Cr^{+6} input concentration increased, breakthrough curves steepened, indicating faster column saturation. This is because mass transfer flow from the solution to the adsorbent surface decreases as the driving force decreases. Higher influent concentrations enhance Cr^{+6} molecule availability, increasing the adsorption rate and decreasing the breakthrough time since the adsorbent bed is saturated sooner [41,42].

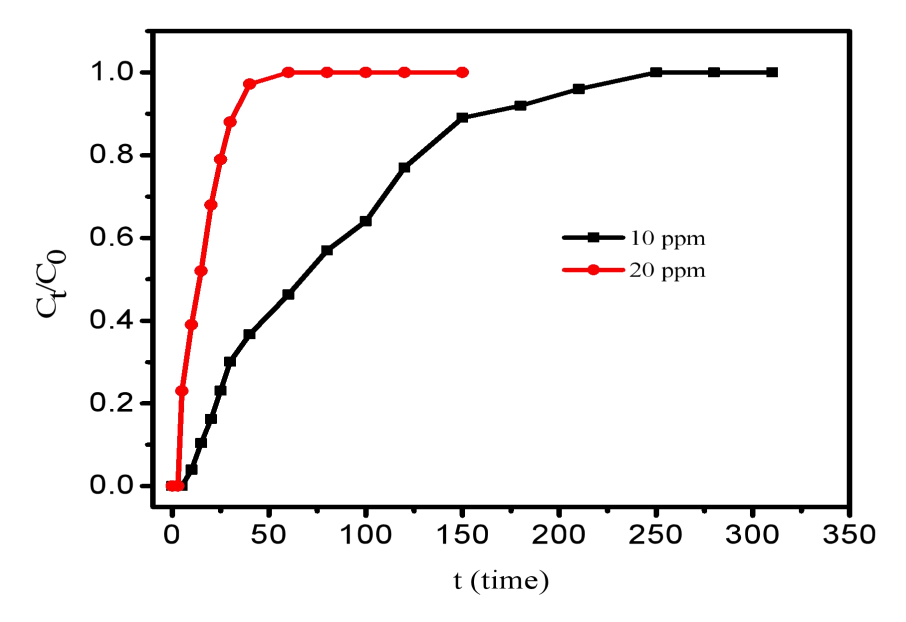


Fig. 12. Breakthrough curves at different initial concentrations (bed depth = 0.5 cm and flow rate = 2.5 ml/min.)

Table 3. Parameters in packed bed column for Cr⁺⁶ biosorption by MNLHH

C ₀ (mg L ⁻¹)	Q (mL/min)	Z (cm)	T _{total} (min)	M _{total} (mg)	Q _{total} (mg)	Q _{e,exp} (mg/g)	V _{eff} (Ml)	L _{MTZ} (cm)
$\frac{\text{(ing 2)}}{10}$	2.5	0.3	100	2.5	0.721	2.404	250	0.288
10	2.5	0.5	250	6.25	1.571	3.142	625	0.473
10	2.5	1	450	11.25	3.018	3.018	1125	0.953
10	2.5	0.5	250	6.25	1.571	3.142	625	0.473
10	3.5	0.5	80	2.8	0.675	1.352	280	0.48
10	2.5	0.5	439	17.56	6.529	13.058	878	0.47
20	2.5	0.5	60	3	0.655	1.312	150	0.473

4. CONCLUSION

The comprehensive characterization and adsorption studies conducted on magnetite nanoparticle-loaded berseem hay (MNLBH) and human hair (MNLHH) revealed their promising potential for Cr⁶ removal from aqueous solutions. The determination of pH_{pzc} indicated that both biosorbents exhibit favourable surface charge properties under acidic conditions, facilitating electrostatic interactions with Cr6+ species. FTIR and XRD analyses confirmed the successful incorporation of magnetite nanoparticles and the presence of key functional groups responsible for adsorption, while TEM imaging demonstrated the spherical morphology and nanoscale size distribution of the particles, ensuring large surface area availability. Batch adsorption experiments showed that both biosorbents achieved maximum Cr⁶ * removal at low pH, with MNLHH slightly outperforming MNLBH in removal efficiency and adsorption capacity. Increasing adsorbent dosage and contact time enhanced removal performance due to the availability of active sites and prolonged interaction periods. Among the applied isotherm models, the Langmuir model best fit MNLBH adsorption, suggesting monolayer coverage, whereas the Temkin model better described the MNLHH system, indicating variable binding energy. Kinetic studies further confirmed the pseudosecond-order model for MNLHH, implying chemisorption, while MNLBH followed the pseudo-first-order model, suggesting physisorption as the predominant mechanism. Fixed-bed column studies reinforced the efficacy of MNLHH in dynamic systems. Increasing bed depth improved breakthrough time and adsorption capacity, whereas higher flow rates and initial concentrations accelerated saturation and reduced performance. These findings underscore the significance of optimizing operational parameters for real-world applications. Overall, this work demonstrates the feasibility and efficiency of using MNLBH and MNLHH as low-cost, eco-friendly biosorbents for Cr⁶ remediation, with MNLHH exhibiting superior adsorption characteristics in both batch and column modes.

Conflict of interest:

The authors declare there are no conflicts.

References:

- 1. Mona A. Abdel-Fatah, Marwa M. Elsayed (2024). Electrochemical Techniques Applied for Industrial Wastewater Treatment: A Review, Egyptian Journal of Chemistry, Vol. 67(4): pp 7-33
- 2. Kebede, F., & Gashaw, A. (2017). Removal of chromium and azo metal-complex dyes using activated carbon synthesized from tannery wastes. Open Access J Sci Technol, 5(2), 1-30.
- 3. Prakash, V., Kumari, K., & Ramakrishnan, V. (2022). Efficient biosorption of hexavalent chromium from water with human hair. ACS omega, 8(1), 915-924.
- 4. Bezza, F. A., & Chirwa, E. M. (2022). Removal of Chromium (vi) Ions from Polluted Water Using Kaolinite Supported Fe/Al Oxide (hydroxide) Composite Nanoadsorbents. CET, *94*, 1453-1458.
- 5. Abo Elazm, A., Abd El-Rahim, W. M., Sabbor, A. T., Moawad, H., & Sedik, M. Z. (2020). Bioremediation of hexavalent chromium widely discharged in leather tanning effluents. Egypt. J. Chem., 63(6), 2201-2212.
- Karnwal, A., & Malik, T. (2024). Nano-revolution in heavy metal removal: engineered nanomaterials for cleaner water. Front. Environ. Sci., 12, 1393694.
- 7. Ebrahiem Esmail Ebrahiem, Riham Adel Mohamed, Mona A. Abdel-Fatah (2022). Novel Electrode Design for Removing CNG Lubricant from Wastewater by Using Electrocoagulation, Egyptian Journal of Chemistry, Vol. 65(8): pp 337-345
- Beagan, A., Khibari, S., & Alswieleh, A. (2023). Magnetic Mesoporous Silica Nanoparticles Functionalized with 5, 5'-Dithiobis (2-Nitrobenzoic Acid) for Highly Efficient Removal of Organic Dyes from Contaminated Water. J. Chem., 2023(1), 4798837.
- 9. Mokif, L. A., Obaid, Z. H., & Juda, S. A. (2024). Synthesis of new composite adsorbents for removing heavy metals and dyes from aqueous solution. *JEE*, 25(6).
- 10. Jamshaid, A., Hamid, A., Muhammad, N., Naseer, A., Ghauri, M., Iqbal, J., ... & Shah, N. S. (2017). Cellulose-based materials for the removal of heavy metals from wastewater—an overview. *ChemBioEng Reviews*, 4(4), 240-256.
- 11. Ghoohestani, E., Samari, F., Homaei, A., & Yosuefinejad, S. (2024). A facile strategy for preparation of Fe3O4 magnetic nanoparticles using Cordia myxa leaf extract and investigating its adsorption activity in dye removal. Scientific Reports, 14(1), 84.
- 12. Oukebdane, K., Necer, I. L., & Didi, M. A. (2022). Binary comparative study adsorption of anionic and cationic azodyes on Fe3O4-bentonite magnetic nanocomposite: kinetics, equilibrium, mechanism and thermodynamic study. Silicon, 14(15), 9555-9568.
- 13. Zhang, H.; Carrillo-Navarrete F.; López-Mesas, M.; & Palet, C. (2020). Use of chemically treated human hair wastes for the removal of heavy metal ions from water. *Water*, 12(5), 1263.
- 14. Jiao, Y.; Han, D. Lu, Y.; Rong, Y.; Fang, L., Liu, Y., & Han, R. (2017). Characterization of pine-sawdust pyrolytic char activated by phosphoric acid through microwave irradiation and adsorption property toward CDNB in batch mode. Desalin. Water Treat., 77, 247-255.
- 15. Essawy, A. A., Sayyah, S. M., & El-Nggar, A. M. (2016). Ultrasonic-mediated synthesis and characterization of TiO 2-loaded chitosan-grafted-polymethylaniline nanoparticles of potent efficiency in dye uptake and sunlight driven self-cleaning applications. *RSC Advances*, 6(3), 2279-2294.
- 16. Rezk, R. A.; Galmed, A. H.; Abdelkreem, M.; Ghany, N. A. & Harith, M. A. (2018). Detachment of Cu (II) and Co (II) ions from synthetic wastewater via adsorption on Lates niloticus fish bones using LIBS and XRF. *J. Adv. Res.*, 14, 1-9.
- 17. Aboussabek, A.; Boukarma, L.; El Qdhy, S.; Ousaa, A.; Zerbet, M. & Chiban, M. (2024). Experimental investigation, kinetics and statistical modeling of methylene blue removal onto Clay@ Fe₃O₄: Batch, fixed bed column adsorption and photo-Fenton degradation studies. *Case. Stud. Chem, Environ. Eng.*, *9*, 100580.
- 18. Das, P., & Chakraborty, V. (2024). Experimental study on removal of chromium using nano-silica coated pyrolysed biochar in batch, fixed bed and fluidized bed reactor: Synthesis, characterization, experimentation and mechanism. *Waste Management Bulletin*, 1(4), 60-66.
- 19. Gh. Al Bazedi, Ehab Abadir, Mona A. Abdel-Fatah (2022). Treatment of Blue HB Reactive Dyes in Textile Wastewater using Bio-waste based Hydroxyapatite, Egyptian Journal of Chemistry, Vol. 65(5): pp 23-31
- 20. Alardhi, S. M.; Albayati, T. M. & Alrubaye, J. M. (2020). Adsorption of the methyl green dye pollutant from aqueous solution using mesoporous materials MCM-41 in a fixed-bed column. *Heliyon*, 6(1).
- Babapoor, A., Rafiei, O., Mousavi, Y., Azizi, M. M., Paar, M., & Nuri, A. (2022). Comparison and Optimization of Operational Parameters in Removal of Heavy Metal Ions from Aqueous Solutions by Low-Cost Adsorbents. *International Journal of Chemical Engineering*, 2022(1), 3282448.
- 22. Juturu, R., Selvaraj, R., & Murty, V. R. (2024). Efficient removal of hexavalent chromium from wastewater using a novel magnetic biochar composite adsorbent. *Journal of Water Process Engineering*, 66, 105908.
- 23. Essawy, A. A., Sayyah, S. M., & El-Nggar, A. M. (2017). Wastewater remediation by TiO2-impregnated chitosan nanografts exhibited dual functionality: high adsorptivity and solar-assisted self-cleaning. *J. Photochem. Photobiol. B. Biol.*, 173, 170-180.

Egypt. J. Chem. 69, No. 2 (2026)

- 24. Chenxi, Y.; Jian, W.; Haiou, Z.; Tingting, C.; Hang, Z.; Jiawei, W. & Bo, B. (2022). Novel fabrication of hydrophobic/oleophilic human hair fiber for efficient oil/water separation through one-pot dip-coating synthesis route. Sci. Rep., 12(1), 7632.
- 25. Olawale, S. A.; Bonilla-Petriciolet, A.; Mendoza-Castillo, D. I.; Okafor, C. C.; Sellaoui, L., & Badawi, M. (2022). Thermodynamics and mechanism of the adsorption of heavy metal ions on keratin biomasses for wastewater detoxification. Adsorpt. Sci. & Technol., 7384924.
- 26. Isik, Z.; Saleh, M.; M'barek, I.; Yabalak, E.; Dizge, N., & Deepanraj, B. (2024). Investigation of the adsorption performance of cationic and anionic dyes using hydrochared waste human hair. Biomass Convers. and Biorefinery, 14(3), 3715-3728.
- 27. Melhi, S. (2023). Amine-Terminated Modified Succinic Acid-Magnetite Nanoparticles for Effective Removal of Malachite Green Dye from Aqueous Environment. Crystals, 13(9), 1301.
- 28. Gill, S. U., Inam, M. A., Iftikhar, R., Nadeem, F., Amjad, H., & Khalid, Z. (2025). Enhanced hexavalent chromium (VI) removal from water using nano zero valent iron modified orange peel powder biochar. International Journal of Environmental Science and Technology, 1-14.
- 29. Sarkar, A., Mushahary, N., Das, B., & Basumatary, S. (2024). A novel approach for modification of montmorillonite using banana peel ash extract for enhanced adsorption efficiency of methylene blue dye. Desalination and Water Treatment, 320, 100585.
- 30. Nyamunda, B. C., Chivhanga, T., Guyo, U., & Chigondo, F. (2019). Removal of Zn (II) and Cu (II) ions from industrial wastewaters using magnetic biochar derived from water hyacinth. Journal of Engineering, 2019(1), 5656983.
- 31. Rezk, R. A., Abdel-Salam, Z., Abdel Ghany, N. A., Abdelkreem, M., & Abdel-Harith, M. (2022). LIBS and pXRF validation for the removal of Pb by bio-CaCO₃ nanoparticles from contaminated water. SN Appl. Sci., 4(5), 151.
- 32. Ali, H. M., Essawy, A. A., Elnasr, T. A. S., Aldawsari, A. M., Alsohaimi, I., Hassan, H. M., & Abdel-Farid, I. B. (2021). Selective and efficient sequestration of Cr (VI) in ground water using trimethyloctadecylammonium bromide impregnated on Artemisia monosperma plant powder.JTiCE,125, 122-131.
- 33. Yuan, J., & Lu, W. (2024). Adsorption of Cr (VI) from aqueous solutions using inorganic clays modified magnetic chitosan adsorbent: Kinetic and thermodynamic study. Desalination and Water Treatment, 319, 100442.
- 34. El-Dakrory, Y.; Sliem, M.; Abdelkreem, M.; Hassab Elnaby, S. & Rezk, R. (2022). Laser induced fluorescence detection of R6G dye adsorbed on Fe₃O₄ nanomaterials. JA WER, 10(4), 322-331.
- 35. Lemessa, G., Chebude, Y., & Alemayehu, E. (2023). Adsorptive removal of Cr (VI) from wastewater using magnetitediatomite nanocomposite. AQUA-Water Infrastructure, Ecosystems and Society, 72(12), 2239-2261.
- 36. Purwiandono, G., & Lestari, P. (2023). Comparison of two biosorbent beads for methylene blue discoloration in water. Journal of Ecological Engineering, 24(8).
- 37. Amode, J. O.; Santos, J. H., Md; Alam, Z.; Mirza, A. H. & Mei, C. C. (2016). Adsorption of methylene blue from aqueous solution using untreated and treated (Metroxylon spp.) waste adsorbent: equilibrium and kinetics studies. Int. J. Ind. Chem., 7, 333-345.
- 38. Syeda, H. I., Muthukumaran, S., & Baskaran, K. (2025). Dynamic adsorption of heavy metals on functionalized and regeneratable biopolymeric aerogels: Fixed-bed column reactor modelling and dual functionality elution technique. Separation and Purification Technology, 131861.
- 39. Das, P., & Chakraborty, V. (2024). Experimental study on removal of chromium using nano-silica coated pyrolysed biochar in batch, fixed bed and fluidized bed reactor: Synthesis, characterization, experimentation and mechanism. Waste Management Bulletin, 1(4), 60-66.
- 40. Marrane, S. E., Dânoun, K., Essamlali, Y., Aboulhrouz, S., Sair, S., Amadine, O., ... & Zahouily, M. (2023). Fixed-bed adsorption of Pb (ii) and Cu (ii) from multi-metal aqueous systems onto cellulose-g-hydroxyapatite granules; optimization using response surface methodology. RSC advances, 13(45), 31935-31947.
- 41. Fernandez, R. M. D., Estrada, R. J. R., Tomon, T. R. B., Dingcong Jr, R. G., Amparado Jr, R. F., Capangpangan, R. Y., ... & Alguno, A. C. (2023). Experimental Design and Breakthrough Curve Modeling of Fixed-Bed Columns Utilizing a Novel 3D Coconut-Based Polyurethane-Activated Carbon Composite Adsorbent for Lead Sequestration. Sustainability 2023, 15, 14344.
- 42. Abdelkreem, M. (2016). Adsorption of phenol from industrial wastewater using olive mill waste. APCBEE procedia, 5, 349-357.